Moncho Esteve, IJ.; Folke, F.; García-Villalba, M.; Palau-Salvador, G. (2017). Influence of the secondary motions on pollutant mixing in a meandering open channel flow. Environmental Fluid Mechanics. 17(4):695-714. https://doi.org/10.1007/s10652-017-9513-4

Influence of the Secondary Motions on Pollutant Mixing in a Meandering Open Channel Flow

Ignacio J. Moncho-Esteve[1] (*Corresponding author*), Frederik Folke[2], Manuel García-Villalba[3], Guillermo Palau-Salvador[1].

[1]Dept. of Rural and Agrifood Engineering, Hydraulic Division, Universitat Politècnica de València, Camino de Vera s/n, 46022 Valencia (Valencia), Spain
igmones@doctor.upv.es
Tlf.: 0034-629936415
Fax: 0034-963877549

[2]Institute for Hydromechanics, Karlsruhe Institute of Technology, Germany
Currently at Federal Waterways Engineering and Research Institute (BAW), Karlsruhe, Germany

[3]Bioeng. and Aeroespace Eng. Dept. Universidad Carlos III de Madrid. 28911 Leganés (Madrid), Spain

Keywords: Large Eddy Simulation; Pollutant Mixing; River Flow; Turbulence.

Abstract

This paper presents large eddy simulation of turbulent flow in a meandering open channel with smooth wall and rectangular cross-section. The Reynolds number based on the channel height is 40,000 and the aspect ratio of the cross-section is 4.48. The depth-averaged mean stream-wise velocity agree well to experimental measurements. In this specific case, two interacting cells are formed that swap from one bend to the other. Transport and mixing of a pollutant is analysed using three different positions of release, *e.g.* on the inner bank, on the outer bank and on the centre of the cross section. The obtained depth-average mean concentration profiles are reasonably consistent with available experimental data. The role of the secondary motions in the mixing processes is the main focus of the discussion. It is found that the mixing when the scalar is released on the centre of the cross-section is stronger and faster than the mixing of the scalar released on the sides. When the position of release is close to a bank side, the mixing is weaker and a clear concentration of scalar close to the corresponding side-wall can be observed in both cases.

Acknowledgements: The simulation was carried out using the supercomputing facilities of the Steinbuch Centre for Computing (SCC) of the Karlsruhe Institute of Technology. The authors would like to thank Clemens Chan-Braun for his valuable and constructive suggestions during the development of this research. MGV acknowledges the financial support of the Spanish Ministry of Education through the program Jose Castillejo.

1 Introduction

The environment is strongly influenced by rivers which form our landscape continuously and are important for the transport of freights. The watercourse of a natural river is often characterized by a curvy shape. The curves are called meanders with inner and outer-banks. Meanders are a result of a complex interaction between sedimentation and erosion processes [1]. They are formed when river flow erodes the outer-banks and widens the river channel. Sediments are transported from the outer to the inner-bank, through which the shape of a river is changed continuously. Due to the effort to handle and regulate rivers, e.g. river restoration, navigability, water quality, production of energy, it is of great importance to understand the various governing mechanisms, including the secondary motions within the meander flow.

The flow in meandering channels is highly three-dimensional and complex, exhibiting secondary motions. The phenomenon of secondary motions was first mentioned by [2] and [3]. They studied the, by now well known, centre-region cell and discussed the influence of secondary motion on the stream-wise velocity distribution and on the sediment transport. Most studies concentrated on this primary cell far from the banks [4–8]. The centre-region cell occurs due to the imbalance between the driving centrifugal force and the transverse pressure gradient [9]. The imbalance introduces a flow from the outer to the inner-bank at the bottom of the channel and a flow from the inner to the outer-bank at the surface of the channel. Due to this cross-stream circulation, sediment is transported from the outer to the inner-bank and cause the typical shape of the bar-pool bed topography around the bends. Mockmore [10] identified, in addition to the classical and relatively well known centre-region cell, a second cell near the outer-bank. This cell, named outer-bank cell, is smaller and weaker than the centre-region cell and rotates in the opposite direction. The mechanism of the two circulation cells underlies the downstream vorticity balance [11]. In this process the centrifugal force and the cross-stream turbulent stresses play a decisive role. Due to the lack of experimental data the mechanism involved in the generation of the outer-bank cell is up to now not fully understood. This makes further investigations of the interactions between the cross-stream circulations and the stream-wise velocity distribution necessary. Blanckaert and

de Vriend [11] and later on van Balen *et al.* [12] suggested that the counter-rotating outer-bank cell is generated from a combination of two mechanisms: the anisotropy of the cross-stream turbulence and the deformation of the vertical profiles of the downstream velocity. W. van Balen [13] suggested that the outer-bank cell could be represented as a Taylor-Görtler vortex through the outer-bank wall. This author analysed term-by-term the balance equation for stream-wise vorticity and figured out that the outer-bank cell is the result of the non-linear interaction between turbulence anisotropy and centrifugal force, which affects the deformed profile of the downstream velocity. Even though the outer-bank cell is smaller and weak, it is of particular importance because it has been related to protect steep outer-banks from erosion [14, 15]. It reduces the level of turbulence activity near the outer bank and so reduces the bank shear stress. Stoesser *at al.* [16] evidenced that the counter-rotating outer-bank cell in a meander bend is the remaining of the centre-region cell of the previous bend. On the other hand, an experimental study on the near-bank hydrodynamic processes in curved open-channel reaches was carried out by [17]. This work revealed two effects of the smaller counter rotating cell: firstly, the cell accentuates the boundary layer on the outer-bank, reducing the strength of the flow on the bank; secondly, the cell also advectes high-momentum fluid toward the bottom of the outer-bank, which gives rise to the strength of the flow on the bank. In addition, the major sapping and local erosion hazard in curved open-channels correspond to the zone where the outer-bank cell has its maximum force, and therefore also the aforementioned protection from erosion. Furthermore, a recent research study [18] of the turbulent flow in a 180 degree sharp open channel bend suggested that the maximum secondary flow strength occurred at the second half of the bend. There have been further studies over the last few years involving natural meandering channels [19–23]. However, a rectangular cross-section reduces the computational cost significantly compared to natural channels and, indeed, it is essential to gain inside in complex physics. A few studies of flow in meandering channels with a simplified geometry can be found [5, 24]. Particularly for the importance of the secondary currents, the lack of understanding of their mechanisms and the influence on mixing, further investigations are needed with an accurate high resolution.

Fischer [25] was among the first who discussed the influence of meandering channel and its secondary motions on the mixing processes. Based on the experimental secondary profiles by [26] and the shear-flow analysis of [27] and [28] he proposed a very strong influence of the secondary motions in meandering rivers on heat and mass transfer, and therefore on the distribution of pollutants. According to his analysis, the lateral spreading of pollutants is increased by the secondary motions due to the higher turbulence intensities. However, Boxall and Guymer [29] argued that the longitudinal spreading is decreased by the same effects. In contrast to [25], Demuren and Rodi [30] argued that in meandering channels convective transport of heat or mass has a stronger effect on the mixing than the turbulence itself. Despite the differences, the authors agree that the mixing process and consequently the effective mixing in meandering channels is very different to that in straight channels. Other study conducted by [31] reviewed the different processes in pollutant mixing in river flows as well as the factors affecting the transverse mixing. The authors stated that secondary currents were found to affect the transverse mixing more than any other factor.

Concerning the modelling of meandering open-channel turbulent flows, a detailed investigation of Booij [32] was not able to correct reproduce the secondary flow motions, especially of the counter-rotating outer-bank cell with Reynolds-averaged Navier-Stokes (RANS) computations. A large eddy simulation (LES) for a meandering channel with rectangular cross-sections was performed by [33]. The authors simulated the open-channel flow in two 180º bends with short cross-over sections connecting these bends. They obtained a very satisfying agreement with the experimental data. In their study, LES was capable to provide detailed information about the time-averaged and the instantaneous flow. A comparison of different turbulence closure approaches by RANS and LES simulations with experiments of the flow in a meandering channel was done by [16]. LES was observed to be superior to RANS. Even though the tested RANS codes were able to simulate the beginning of the outer-bank cell, its evolution until the exit of the bend was not correctly reproduced. Moreover, comparison of experiments, LES and RANS simulations of flows in a curved open-channel bend were presented by [13]. This study shows again that, generally, LES provides much better results than RANS. In addition, the simulated flow pattern

was not very sensitive to the sub-grid model in the LES simulation. This points out that the large scales of turbulence play an important role in the flow processes, which interact with the mean secondary motions. Moreover, a high-resolution LES of turbulent flow in a natural meandering channel with pool-riffle sequences was employed to clarify the hydrodynamics of such specific conditions [34]. This model was higher resolution than previous works, so it could capture the mechanism of formation of two cell system in the meander bend. On the other hand, an investigation on the characteristics of turbulent flow in a meandering open-channel bend based on LES was carried out by [35]. Even though the grid resolution was somewhat coarse, the simulation results were validated by means of experimental measurements and good agreement was achieved.

In this paper, a LES is performed using the same flow configuration of the laboratory meander with rectangular cross-sections studied by [24]. Focus is given to the three-dimensional secondary motions and its influence in the mixing processes using three different positions of release, i.e. inner bank, outer bank and centre of the cross section. This case was studied previously by [36] in the context of a RANS simulation.

2 Flow Configuration

The experiments of Chang [24] were carried out in a small flume with smooth wall and rectangular cross-section through seven consecutive meanders. The cross-section (B) was 0.254 m wide and the water level (h) was at 0.057 m (Fig. 1a). The total length of the channel measured along the centreline was 25.91 m. The seven meanders consist of 13 identical 90°-bends (curvature radius of 0.914 m) in alternate directions linked with straight sections of 0.476 m length and a bottom slope of 0.0012. The velocity measurements were performed with a 1.588 mm standard Prandtl-type pitot tube.

The dispersant used for this study was neutrally buoyant solution obtained by mixing salt water and methanol. It was injected by a right-angle 3.175 mm brass tube, connected by a Tygon tube to a funnel hanging beneath the orifice as a continuous point source. The discharge was located in the eighth bend at Section 8C (Fig. 1b) at three different positions in mid-depth: right bank

(RB), left bank (LB) and centre line (CL) and whereby the RB and LB was 0,0254 m away of their respective channel wall. The three scalars are named as S1, S2 and S3, respectively.

3 Numerical Model

For a LES, the incompressible Navier-Stokes equations are filtered, here the following equations are resulting:

$$\frac{\partial \overline{U_i}}{\partial x_i} = 0 \tag{1}$$

$$\frac{\partial \overline{U_i}}{\partial t} + \frac{\partial \overline{U_i}\,\overline{U_j}}{\partial x_j} = \frac{1}{\rho}\frac{\partial \overline{p}}{\partial x_i} + \nu \frac{\partial^2 \overline{U_i}}{\partial x_j^2} - \frac{\partial \tau_{ij}^{SGS}}{\partial x_j}, \tag{2}$$

whereby $\overline{U_i}$ and $\overline{p}$ are the resolved filtered velocity and pressure and τ_{ij}^{SGS} are the sub-grid scale (SGS) stresses

$$\tau_{ij}^{SGS} = \overline{U_i U_j} - \overline{U_i}\,\overline{U_j} \tag{3}$$

They represent the influence of the small unresolved scales to the large resolved scales. These are unknown and have to be modelled.

The LES was performed with the in-house code LESOCC2 (Large Eddy Simulation On Curvilinear Coordinates). It is a successor of the code LESOCC developed by Breuer and Rodi [37] and it is described by Hinterberger [38]. The code solves the Navier-Stokes equations on body-fitted, curvilinear grids using a cell-centred finite volume method with collocated storage arrangement for the Cartesian velocity components. Second-order central differences are employed for the convection as well as for the diffusive terms. The time integration is performed with a predictor-corrector scheme, where the explicit predictor step for the momentum equations is a low-storage three-step Runge-Kutta method. The corrector step covers the implicit solution of the Poisson equation for the pressure correction (SIMPLE). The Rhie and Chow momentum interpolation [39] is applied to avoid pressure-velocity decoupling. The Poisson equation for the pressure increment is solved iteratively by means of the “strongly implicit procedure” of Stone [40]. Parallelization is implemented via domain decomposition, and explicit message passing is used with two halo cells along the inter-domain boundaries for intermediate storage.

The subgrid-scale (SGS) stresses, resulting from the unresolved motions, are modelled using the Smagorinsky subgrid-scale model [41] with a model constant C_s=0.1. Such an approach has been used successfully for similar flows by Hinterberger et al. [42]. For flows without homogeneous directions, as the present one, the Smagorinsky model is more robust than other models like the dynamic Smagorinsky which require some kind of smoothing of the model parameter (like time relaxation). Near the walls Van-Driest damping is employed.

For the numerical calculation a global coordinate system was used (*X*, *Y*, *Z*), while for the data analysis the quantities were transformed on a body-fitted coordinate system. The *x*-axis is hereby along the centreline of the channel bed, the *y*-axis along the span-wise and the *z*-axis along the vertical direction. The Reynolds number based on the bulk velocity and the water depth is 40,000. The cross-sectional aspect ratio of channel width to water depth is 4.48. The computational grid consists of $448 \times 169 \times 58 = 4.4 \cdot 10^6$ grid points in *x*-, *y*- and *z*-direction respectively.

The computational grid is uniform along the centreline in *x*-direction and stretched in *y*- and *z*-direction to achieve a better resolution of the near wall motions. The grid sizes in terms of wall units are $\Delta y^+ = \Delta z^+ \approx 13$ near the walls and a maximum value of $\Delta x^+ \approx 340$ in stream-wise direction. The stretching ratio is kept to a fix value of 1.03. For the sake of clarity only the grid in the left half of a cross-section of the full domain is shown in Fig. 1b (top). A periodic boundary condition is defined for the flow conditions at the inflow and outflow sections of the meander. The Werner-Wengle wall model was employed at the bottom boundary and lateral walls jointly with a rigid-lid assumption for the free surface. Although the wall units could be regarded as coarse, it is accounted by the use of wall functions. A coarse grid was used in a previous work [35] in the same way as we have done.

In addition to the flow field, concentration fields due to tracer discharge from point sources have been simulated. Therefore, an additional transport equation is solved for each of the passive scalars using the bounded HLPA scheme [43] for the convection term in this equation. An eddy diffusivity model was employed to account for the subgrid-scale contribution with a turbulent Schmidt number of 0.6. This approach for the passive scalar modelling has been employed

successfully in previous studies for other complex flows [44–47]. For the molecular Schmidt number a value of 1 was used. For the transport equation, a convective outlet condition was imposed, a homogeneous Dirichlet condition was imposed at the inlet and homogeneous Neumann conditions were imposed at all other boundaries.

The tracer injection points are chosen to match the experimental setup [24]. The injection points are located in the section 8C as displayed in Fig. 1b. In the simulation, an iso-kinetic discharge is used for simplicity of implementation: in a group of cells the tracer concentration is set to 1 and the tracer acquires the velocity of the flow at that location. The injection in the experiment was not iso-kinetic with an injection velocity of the order of the velocity in the free-stream.

After discarding initial transients, averages are collected until first and second order statistics are well converged.

4 Results and Discussion

4.1 Stream-wise Flow

The depth-averaged mean stream-wise velocity $\overline{u}^h$ of the flow is shown in Fig. 2. All velocities are normalized by the average velocity over the cross-section defined as $U_s=Q/A_s$, where Q is the discharge and A_s is the cross-sectional area ($A_s = h \cdot B$). As the curvature changes the region of high velocity shifts across the channel. According to the literature [48], the highest velocities in a meandering channel are expected to occur at the inner-bank. The results of the simulation confirm this expectation as shown in Fig. 2a. At Sections 9A and 10A, in the middle of the bends, the maximum velocity occurs near the inner walls. At Sections 9B and 10B, the maximum velocity still occurs at the inner-banks, however, it is a little shifted towards the channel centre. In Sections 8C and 9C, where the channel has zero curvature the maximum velocity is found close to the channel centre, followed by Sections 8D and 9D, where the maximum velocity has shifted to the opposite bank, now being the inner part. A comparison of the depth-averaged stream-wise velocity with the experiments is given in Fig. 2b. At eight different locations the velocity profile along the span-wise direction is compared to the experimental data obtained by [24]. The

agreement is very satisfying, except close to the wall where some deviations can be recognized. The deviation may stem from the steep gradient that exists in this region as well as from the sensitivity of the profile on small deviations along the centreline. Moreover, the measurements near the walls can be difficult to take in the experiments which should add uncertainty. The good agreement with the stream-wise flow supports the assumption that the grid resolution is sufficient to capture major effects in the flow field.

4.2 Secondary Motions

Secondary motions are very important to understand the mixing processes within the meander [25]. To analyze in detail the evolution of these secondary motions, mean cross-stream velocity vectors at the selected sections (Fig. 1a) are presented in Fig. 3. Velocities are normalized by the aforementioned sectional velocity U_s.

In Section 8C, a big anti-clockwise recirculation cell can be observed near the inner bank (right lateral wall). This dominant cell is clearly visible with a centre located at y/h=3.5 and z/h=0.6. While the flow near the bed moves from the outer to the inner-bank (left to right), the flow close to the surface moves in the opposite direction. In addition to the primary cell a small cell near the outer-bank (left lateral wall) is present, rotating in a clockwise direction. The centre of this secondary cell is hereby located at y/h=0.5 and z/h=0.8. The flow at the bottom of the channel has already switched sign at Section 8D. In this position, the small cell rotating in clockwise direction mentioned above becomes the dominant cell. Close to the surface of the inner-bank, rotating in an anti-clockwise direction, the previous primary cell can be seen with decreasing strength. In Section 9A and Section 9B this anti-clockwise cell is still occurring but it is losing momentum downstream in the channel bend. However, the clockwise cell seems stronger in Section 9A and 9B, compared to Section 8D.

Further downstream, the dominant clockwise cell of the upstream channel bend is still clearly visible with a centre located at y/h=0.5 and z/h=0.6 in Section 9C, which is placed in the middle of the straight channel section (Fig. 1a). In this case, the flow near the bed moves from the right to the left-bank. Again, a small secondary cell (right lateral wall) is present but with an anti-

clockwise direction. The centre of the small cell is located at y/h=4 and z/h=0.8. The next section shown, Section 9D, is situated at the beginning of the next bend, where the left lateral wall is now the inner-bank. Just as occurred at Section 8D, the flow at the bottom of the channel has already switched sign. The small cell rotating in anti-clockwise direction mentioned above becomes the dominant cell. Close to the surface in the inner-bank, rotating in clockwise direction, the previous primary cell is decreasing in strength again. As we move downstream, the cycle is repeated and the anti-clockwise cell is increasing in strength while the small counter-rotating cell is decreasing again (Section 10A and Section 10B). The maximum lateral velocity throughout the meander is found in the bends, from the apex to the exit (Sections 9A-B and Sections 10A-B), with a magnitude of $0.20U_s$ near the bed. Except from these areas, the magnitude of the lateral velocity is less than $0.13U_s$ in most sections. The lateral velocity is generally stronger than the vertical velocity. The vertical component of velocity has its higher values near the walls, with a positive sense and a magnitude of about $0.1U_s$ in the latter half of the bends. It is possible to figure out a feed-back (*i.e.* the exchange of fluid) between these two cells along the meander while the major cross-stream momentum is found at the bottom of the channel and the separation between such recirculation cells. Furthermore, in line with the secondary flow structure described by [6] it is possible to distinguish a growth and decay of these two main recirculation cells throughout the meander.

The presence of the primary cell as well as the smaller counter-rotating cell are in agreement with previous studies [6, 14, 15]. A direct validation via experimental data is not possible because not all velocity components were measured in the experiments of Chang [24]. However, the results obtained with the LES simulation are consistent with the velocity vectors in cross-stream planes computed by Demuren and Rodi [36]. Although that RANS simulations [36] were able to clearly define a large recirculation, this was not the case with the counter-rotating cell. Moreover, we obtain a more detailed description of the dominant cell and the counter-rotating cell (Fig. 3). In addition, the higher resolution provides a more comprehensive picture of the growth and decay of the secondary motions through the meander and the exchange of fluid between them.

4.3 Transverse Mixing

Contours of the depth-averaged mean concentration $\overline{C}^h$ distribution are shown in Fig. 4. It can be seen how the scalar remains close to the walls when the position of release is nearby the bank sides (S1 and S2). A higher concentration of scalar seems to be obtained until the end of the next bend for the release in the right bank (S1). This should be due to the evolution of the anti-clockwise recirculation cell (Fig. 3) from the section of release (right lateral wall), as just described in the previous section, and the tendency to the flow to accelerate near the inner wall and to decelerate near the outer wall of the bends. In contrast, when the scalar is discharged at the centreline of the channel (S3), concentration is significantly reduced by the end of the first bend due to the effect of the secondary motions and its feed-back between the primary cell and the secondary cell.

The depth-averaged mean concentrations for the three different positions of release are shown in Fig. 5. As it was calculated by Chang [24], the concentrations are normalized with the local mean concentration defined as:

$$\overline{C}^s = \frac{h}{Q}\sum_{j=1}^{n} \overline{C}_j^h \, \overline{u}_j^h \, \Delta y \qquad (4)$$

with, *h*, the water depth, *Q*, the flow discharge, $\overline{C}_j^h$, the depth-average mean concentration, $\overline{u}_j^h$, the depth-averaged mean stream-wise velocity. Hereby, the sum over all the positions *j* in span-wise direction and Δy the corresponding span-wise grid size are computed. The strongest mixing is obtained when the position of release is at the centre line (S3) (Fig. 5e,f). Due to the presence of the dominant cell the scalar strongly enhances mixing throughout the cross section and a nearly uniform depth-average mean concentration profile is obtained at section 9D. When the position of release is close to the bank sides, the mixing is weaker and a clear concentration of scalar close to the corresponding side wall can be observed in both cases. However, slightly major dilution seems to be obtained for the release on the left bank (S2) (Fig. 5c,d), with maximum peak differences between simulation cases S1 and S2 of about $\overline{C}^h / \overline{C}^s$ = 0.6 in section 9B and 0.2 in

section 9C. One possible reason could be the presence of the small clockwise cell near the S2 injection at Section 8C (Fig. 3), which becomes the dominant cell at Section 8D, enhancing mixing. On the other hand, when the scalar is released near the right wall (S1) (Fig. 5a,b) in Section 8C, the injection is done very close to the centre of the big anti-clockwise recirculation cell observed beside the inner bank. However, as it was mentioned previously, this primary cell has decreased in strength at Section 8D, and this may retain spreading until Section 9D, when the flow at the bottom of the channel switches sign. At this time, the small cell dominating S1 distribution mentioned above becomes the dominant cell and eventually increases in strength.

As it can be seen in Fig. 5, the predicted depth-average mean concentration profiles show good agreement with the measurements for the S2 and S3. Although the trends of the profiles are reasonably reproduced by the model for S1, significant differences were found in all the tested sections, especially in the peak values. These computed data are rather similar to the above-mentioned results obtained by [36]. When the scalar is released near a wall, the simulation tends to overestimate concentrations near this wall while it is underestimated in the opposite one. This is more dramatic for the S1 than for the S2. Conversely, in the case of S3 concentrations are slightly underestimated.

There could be several reasons to explain the discrepancies between experimental data and the present results. For instance, there is a fundamental difference in the way in which the depth-averaged quantities were obtained. The experimental depth-averaged mean concentration is based on measurements only at three depths at each span-wise position while the LES computations are carried out with the average over 58 vertical grid points. Therefore, this might affect considerably the depth-averaged mean concentration calculation in these cases and lead to discrepancies between the experimental and computed profiles. Note also that the profiles are normalized with the mean concentration averaged over the section. The determination of this quantity is done in the experiments using 20 span-wise locations at 3 depths while for our data we do it using the whole grid (169x58 points). We have evaluated the local mean concentration in each section using the same points as in the experiment. The largest differences are found in Section 9B, where the

discrepancies with respect to the local mean concentration obtained with the whole grid are 3% for S3, 7% for S2 and 15% for S1.

In addition, Demuren and Rodi [36] pointed out that curvature effects acting on the sidewall boundary layers can have little influence on the eddy diffusivity in this case. Thus, how turbulence is modelled here and how this may be dominated by the boundary layers of the sidewalls owing to the relatively low depth to width ratio and smooth wall appears to affect the concentration distribution in the simulations. Furthermore, in the LES, an iso-kinetic release is used and the tracer acquires the velocity of the flow at the location. In the experiments, the injection velocity is of the same order as the velocity in the free-stream. This means that the experimental injection velocity should be different than computed velocity at the release points. In addition, in the experiments, the scalar was injected by a brass tube which should be affecting the flow. In view of the above, these differences might lead to significant variations in the initial development of the tracer concentration compared to experimental profiles, as was the case in [45].

Moreover, In the case of S1, the scalar is discharged near the inner-bank entering the bend, where the highest velocities are expected to occur, promoting transport downstream. Moreover, LES velocity values are slightly overestimated next to the bank sides (see Sections 9A and 9B in Fig. 2b). In Section 9A and Section 9B the anti-clockwise cell in the right side is losing momentum downstream in the channel bend which means less spreading. On the other side, the scalar S2 is injected near the outer-bank entering the bend, where the lower velocities are expected to occur, retaining transport downstream. As it was suggested above, the anti-clock wise recirculation is increasing along the bend and this should promote dilution of S2. These aspects seem to suggest a significant influence of the secondary currents on the mixing and the important interaction with the stream-wise velocity profile.

In addition, in Fig. 6, the mean concentration $<C>$ field is shown at 7 different planes along the meander. The concentrations are normalized with the area-weighted average of the mean concentration C_s on each section. On the left and the middle columns, the evolution of the scalar released at the outer and inner bank is shown. The effect of the secondary motions on the mixing process and on the evolution of the dominant cell is clearly visible. Additionally, the maximum

value observed in the S1 concentration correlates with the shift of the maximum stream-wise velocity from the inner to the outer bank (Fig. 2a). On the other hand, the right of the figure shows the evolution of the concentration when the release is located at the centre line. Clearly, the mixed process is higher due to the effect of secondary motions. From Section 9A to 9C it is possible to see the influence of the primary cell on the maximum values of S3. At the same sections, the small counter-rotating cell tends to keep without mixing the right side. Afterwards, the flow at the bottom of the channel switched sign and in less than two bends (section 10B) contour field is almost uniform in the whole section which agrees well with the experimental results from Chang [24]. The aforementioned momentum at the separation between the cross-stream recirculation cells and the feed-back between them seem to play an important role in the mixing of this release.

4.4 Quantification of Mixing

The coefficient of variation was proposed and obtained by Chang [24] as:

$$C_v = \frac{1}{\overline{\overline{C}}} \sqrt{\frac{1}{n} \sum_{j=1}^{n} (\overline{C}_j^h - \overline{\overline{C}})^2} \tag{5}$$

where $\overline{\overline{C}} = \frac{1}{n} \sum_{j=1}^{n} \overline{C}_j^h$. C_v can be seen as a good indication of the level of mixing along the *x*-axis.

Many different indices for assessing mixing efficiency have been introduced in the literature. Denev *et al*. [44] studied several of them in their analysis of a swirling jet in a cross flow. Although in principle these indices quantify different aspects of mixing, the analysis of Denev *et al*. [44] shows that similar trends were obtained for the indices considered. In particular, the spatial mixing deficiency (SMD) at a given *x* is defined as:

$$SMD = \frac{rms[<C>-av(<C>)]}{av\ (<C>)} \tag{6}$$

where $< C >$ is the time-averaged concentration, *a*v and *rms* represent space-averaging and root-mean-square within the cross-section. Thus, SMD measures uniformity in space and seems to be rather similar to the aforementioned coefficient of variation, which confirms so far the validity of the index proposed by Chang. Since it is intended to compare the original experimental data with

the simulations, we have selected the C_v for this analysis. Figure 7 shows a comparison between the experimental and the computed C_v for the three scalar injections. The predicted coefficient of variation shows reasonable agreement with the measurements for the three release locations. C_v tends to fall downstream along the meander for all cases, indicating mixing due to the complex flow behaviour described above. The results of the coefficient show that the mixing with the centre-line release is much faster than the others. The scalar released close to the inner bank (S1) and the outer bank (S2) show relatively similar values and behaviour. On the other hand, higher values are observed for S1 until Section 10A. From this section, however, higher values are observed for S1 in comparison with S2.

Furthermore, as it was done by Palau-Salvador *et al.* [45], in order to complement the qualitative results described above, we now try to quantify the spreading and dilution of the plumes of the scalar along the stream-wise x direction of the meander. Therefore, at every location along the x-axis we define the half-section of concentration S as the area where the concentration is larger than $0.5C_{max}$, where C_{max} is the time-averaged maximum concentration at each x section. The evolution of the half-section S, non-dimensionalized with the cross-sectional area A_s, for the three tracer injections considered is shown in Fig. 8a. In addition, Fig. 8b displays the decay of the time-averaged maximum concentration C_{max}.

The results of the half-section S evolution shows that the spreading of the plume is similar for the three scalar releases until $x/h \approx 15$, located between Sections 8D and 9A. The plume of scalar S3 seems to grow faster than the others, which confirms the results described in the previous sections. Between the Section 8D and the Section 9C, the evolution of the plume seems to be reasonably constant. The shifts in the secondary motions and its feed-back between the primary cell and the counter-rotating cell in between Sections 9C and 9D should induce a slight change in the trend. The half-section S reaches the maximum value of 1, before $x/h = 50$, indicating that the half-section S covers the whole domain, *i.e.* complete mixing under our half-section definition.

Between Sections 9A and Section 9C the half-section of the plume for S2 is slightly higher than S1, which should be related to the dominant clockwise recirculation cell through these sections (Fig. 3). Up to this Section 9C, the anti-clockwise cell near the right bank is decreasing in stream-

wise direction and seems to retain spreading of S1. From then on, half-section *S* development of the right bank release, S1, shows that the dilution of the plume occurs more quickly than for the left bank release, S2 , which seems to keep spreading almost constant until about $x/h = 55$. This mechanism should be controlled by the shift in the velocity structures observed between Section 9C and 9D (Fig. 3). The small anti-clockwise cell dominating S1 distribution now becomes the dominant cell and begins to increase in strength while the clock-wise cell is decreasing again. Given the above, the growth and decay of the primary cell and the small counter-rotating cell and its evolution downwards appear to be a significant mechanism controlling mixing when the injection is done near the banks.

Finally, concerning the value of the plume's maximum concentration displayed on Fig. 8b, it can be seen that the scalar injections close to bank sides (S1 and S2) have a similar maximum value along the meander. On the other hand, the plume's maximum concentration of the scalar discharged in the centre of the channel (S3), behaves in a different way than the other two tracer release, showing the minimum concentrations at all times. As we have just been discussing, this should be due to the effect of the secondary motions and the feed-back between the primary cell and the counter-rotating cell, causing a greater mixing in this case.

4.5 Analysis of Fluctuations

In this section a closer look to the instantaneous flow, instantaneous concentration fields and turbulence statistics of scalar quantities is given. Figure 9 shows a comparison of the instantaneous stream-wise velocity u, the instantaneous secondary flow vectors (both normalized with the bulk velocity U_s) and the instantaneous concentration C field which is normalized with the aforementioned area-weighted average of the mean concentration C_s. For the sake of brevity, only three planes along the channel are shown, namely at the bends apex Sections 9A and 10A and in the cross-over region section 9C. In the inner-bank region (right half of the Section 9A and left half of the Section 10A) higher velocities are occurring and the maximum is shifted along the bend in downstream direction to the centre region. But in the instantaneous flow also a large amount of turbulence is evident and the flow appears much less organized and more unstructured. Over the

whole cross-section turbulent motions can be detected in the contour plot (Fig. 9a). In reference to the normalized instantaneous concentration fields (Fig. 9c,d,e), a high spatial variability can be seen. In agreement to the mean concentration contour fields (Fig. 6), it can be seen how the strongest mixing is obtained when the position of release is at the centre line (S3). On the other hand, it is possible to see the influence of the secondary motions not only in the stream-wise flow, but also in the spreading of the scalars. For example, if we look at Fig. 9b (left), near the position $y/h \approx 2.2$ and $z/h \approx 0.5$, there is a clockwise recirculation cell and by the right side of this, $y/h \approx 2.6$ and $z/h \approx 0.9$, an anti-clockwise cell. Near the same position in Fig. 9a (left), the contour of u is influenced by the outer perimeter of these two structures. As regards to instantaneous concentration fields, the contours of the S2 and S3 (Fig. 9d,e (left)) are clearly influenced by the abovementioned cells. Once again, these relations seem to suggest an important influence of the secondary motions on the mixing and the interaction with the stream-wise velocity.

Figure 10 shows contours of the root mean square concentration fluctuations C^{rms} at 7 different planes along the meander. The fluctuations are normalized with the area-weighted average of the mean concentration C_s on each section. In all three releases, the fluctuations are located in a region close to each contour plume (Fig. 6) with similar recognizable patterns until the end of the first curve (Section 9B). Thus, the fluctuations remain close to the walls when the position of release is nearby the bank sides (S1 and S2). Otherwise, in the case of S3, fluctuations are significantly reduced by the cross-over region (Section 9C). However, towards the second half of the second curve (Section 10A and 10B), while the maximum mean concentrations of S1 and S2 remain close to the lateral walls (Fig. 6)their C^{rms} are higher in the middle section.

At every location along the x-axis we define the half-section S^{rms} as the area where $C^{rms} > 0.5\, C^{rms}_{\max}$. Profiles of half-section S^{rms} and $C^{rms}_{\max}$ as a function of x are shown in Figs. 11a and b, respectively. The trends observed for the maximum mean concentration (Fig. 8b) and discussed in the previous section are similar to the concentration fluctuations (Fig. 11b), with a predominance of maximum fluctuations for S1. The half-section S^{rms} profiles of tracer injections S3 displays a similar tendency, growing quickly until the entrance of the second curve (near Section 9D), Fig. 11a, and presenting

in general higher values than the half-section S^{rms} profiles of tracer injections S1 and S2. Towards the end, the half section of S3 tends to decline, however, for the last two stations considered, the C^{rms} of S3 is rather homogeneous (see Fig. 10) so that the meaning of this quantity in such a situation is questionable.

5 Conclusions

In this paper the results of a large eddy simulation of the flow and the mixing process in a meandering channel were presented. Three different positions of release in mid-depth for a passive scalar have been compared. In agreement with previous studies, the maximum of the depth-averaged mean stream-wise velocity occurred at the inner-bank in each channel bend. The comparison with experimental data of the depth-averaged mean stream-wise velocity was very satisfying. In addition, the simulated depth-averaged mean concentration profiles show acceptable agreement with the measurements for the three release locations. The main focus was on the development of the secondary motions and their possible implications on pollutant mixing in meandering currents. In the simulation the distribution of the mean concentration could be determined throughout the computational domain while in the experiment only a few planes could be measured. Moreover, a closer look to the instantaneous flow, instantaneous concentration fields and turbulence statistics of scalar quantities was given. Therefore, it was possible to obtain further physical insights from the computed data.

It was shown that, for this particular case, two interacting cells are formed that switch from one bend to the other. In spite of the low strength of the cells, they influence considerably the transport and the lateral mixing of pollutants. Moreover, the spreading of the passive scalar is strongly dominated by the primary cell. As a result, the mixing of the scalar released on the centre of the cross-section is stronger and faster than the mixing of the scalar released on the sides, due to the effect of the cross-stream recirculation cells and the feed-back between them. When the position of release is close to a bank side, a clear concentration of the scalar remains close to the wall. The switch of the primary cell and the small counter-rotating cell and its evolution downwards appear to play an important role in mixing when the injection is done near the banks.

References

1. Julien PY, Duan JG (2005) Numerical Simulation of the Inception of Channel Meandering. Earth Surf Process Landf J Br Geomorphol Res Group 1093–1110.

2. Boussinesq J (1868) Mémoire sur l'influence des frottements dans les mouvements reguliers des fluids. J Math Pures Appl 13:377–424.

3. Thomson J (1876) On the origin of windings of rivers in alluvial plains, with remarks on the flow of water round bends in pipes. Proc R Soc Lond 25:5–8.

4. Booij R, Tukker J (1996) 3-Dimensional Laser-Doppler Measurements in a Curved Flume. In: Adrian RJ, Durão DFG, Durst F, Heitor MV, Maeda M, Whitelaw JH (eds) Dev. Laser Tech. Appl. Fluid Mech. Springer Berlin Heidelberg, pp 98–114

5. Muto Y (1997) Turbulent flow in two-stage meandering channels. Ph.D., The University of Bradford

6. Shiono K, Muto Y (1998) Complex flow mechanisms in compound meandering channels with overbank flow. J Fluid Mech 376:221–261. doi: 10.1017/S0022112098002869

7. Tominaga A, Nagao M, Nezu I (1999) Flow structure and momentum transport processes in curved open-channels with vegetation. Proc 28th IAHR Congr.

8. Booij R (2003) Measurements and large eddy simulations of the flows in some curved flumes. J Turbul 4:N8. doi: 10.1088/1468-5248/4/1/008

9. Jia Y, Blanckaert K, Wang SS (2001) Numerical simulation of secondary currents in curved channels. Proc 8th FMTM-Congr.

10. Mockmore C (1943) Flow Around Bends in Stable Channels. Trans ASCE 3:334–334.

11. Blanckaert K, De Vriend HJ (2004) Secondary flow in sharp open-channel bends. J Fluid Mech 498:353–380. doi: 10.1017/S0022112003006979

12. Balen WV, Uijttewaal WSJ, Blanckaert K (2009) Large-eddy simulation of a mildly curved open-channel flow. J Fluid Mech 630:413–442. doi: 10.1017/S0022112009007277

13. Balen W van, Blanckaert K, Uijttewaal WSJ (2010) Analysis of the role of turbulence in curved open-channel flow at different water depths by means of experiments, LES and RANS. J Turbul 11:N12. doi: 10.1080/14685241003789404

14. Christensen HB (1999) Secondary turbulent flow in an infinte bend. Iahr Symp. River Coast. Estuar. Morphodynamics

15. Blanckaert K, Graf WH (2004) Momentum Transport in Sharp Open-Channel Bends. J Hydraul Eng 130:186–198. doi: 10.1061/(ASCE)0733-9429(2004)130:3(186)

16. Stoesser T, Ruether N, Olsen NRB (2010) Calculation of primary and secondary flow and boundary shear stresses in a meandering channel. Adv Water Resour 33:158–170. doi: 10.1016/j.advwatres.2009.11.001

17. Blanckaert K, Duarte A, Chen Q, Schleiss AJ (2012) Flow processes near smooth and rough (concave) outer banks in curved open channels. J Geophys Res Earth Surf 117:F04020. doi: 10.1029/2012JF002414

18. Vaghefi M, Akbari M, Fiouz AR (2016) An experimental study of mean and turbulent flow in a 180 degree sharp open channel bend: Secondary flow and bed shear stress. KSCE J Civ Eng 20:1582–1593. doi: 10.1007/s12205-015-1560-0

19. Kang S, Lightbody A, Hill C, Sotiropoulos F (2011) High-resolution numerical simulation of turbulence in natural waterways. Adv Water Resour 34:98–113. doi: 10.1016/j.advwatres.2010.09.018

20. Engel FL, Rhoads BL (2016) Three-dimensional flow structure and patterns of bed shear stress in an evolving compound meander bend. Earth Surf Process Landf 41:1211–1226. doi: 10.1002/esp.3895

21. Khosronejad A, Hansen AT, Kozarek JL, Guentzel K, Hondzo M, Guala M, Wilcock P, Finlay JC, Sotiropoulos F (2016) Large eddy simulation of turbulence and solute transport in a forested headwater stream. J Geophys Res Earth Surf 121:2014JF003423. doi: 10.1002/2014JF003423

22. Mera I, Franca MJ, Anta J, Peña E (2015) Turbulence anisotropy in a compound meandering channel with different submergence conditions. Adv Water Resour 81:142–151. doi: 10.1016/j.advwatres.2014.10.012

23. Termini D (2015) Momentum transport and bed shear stress distribution in a meandering bend: Experimental analysis in a laboratory flume. Adv Water Resour 81:128–141. doi: 10.1016/j.advwatres.2015.01.005

24. Chang Y (1971) Lateral mixing in meandering channels. Ph.D., The University of Iowa

25. Fischer HB (1969) The effect of bends on dispersion in streams. Water Resour Res 5:496–506. doi: 10.1029/WR005i002p00496

26. Rozovskii IL (1957) Flow of water in bends of open channels. Isr Progr Sc Transl

27. Taylor G (1954) The Dispersion of Matter in Turbulent Flow through a Pipe. Proc R Soc Lond Math Phys Eng Sci 223:446–468. doi: 10.1098/rspa.1954.0130

28. Elder JW (1959) The dispersion of marked fluid in turbulent shear flow. J Fluid Mech 5:544–560. doi: 10.1017/S0022112059000374

29. Boxall JB, Guymer I (2003) Analysis and Prediction of Transverse Mixing Coefficients in Natural Channels. J Hydraul Eng 129:129–139. doi: 10.1061/(ASCE)0733-9429(2003)129:2(129)

30. Demuren AO, Rodi W (1984) Calculation of turbulence-driven secondary motion in non-circular ducts. J Fluid Mech 140:189–222. doi: 10.1017/S0022112084000574

31. Sharma H, Ahmad Z (2014) Transverse mixing of pollutants in streams: a review. Can J Civ Eng 41:472–482. doi: 10.1139/cjce-2013-0561

32. Booij R (1995) Eddy Laser Doppler measurements and turbulence modeling of the flow in a curved flume. Proc 1995 ASMEJSME Fluid Eng 6 Th Int Laser Anemometry Conf Laser Anemometry Hilton Head SC

33. Stoesser T, Ruether N, Olsen N (2008) Near-bed flow behavior in a meandering channel. RiverFlow 2008 4th Int. Conf. Fluv. Hydraul.

34. Kang S, Sotiropoulos F (2011) Flow phenomena and mechanisms in a field-scale experimental meandering channel with a pool-riffle sequence: Insights gained via numerical simulation. J Geophys Res Earth Surf 116:F03011. doi: 10.1029/2010JF001814

35. Xu D, Bai Y, Munjiza A, Avital E, Williams J (2013) Investigation on the Characteristics of Turbulent Flow in a Meandering Open Channel Bend Using Large Eddy Simulation. Proc. 2013 IAHR World Congr.

36. Demuren AO, Rodi W (1986) Calculation of flow and pollutant dispersion in meandering channels. J Fluid Mech 172:63–92. doi: 10.1017/S0022112086001659

37. Breuer M, Rodi W (1994) Large-Eddy Simulation of Turbulent Flow through a Straight Square Duct and a 180° Bend. In: Voke PR, Kleiser L, Chollet J-P (eds) Direct Large-Eddy Simul. I. Springer Netherlands, pp 273–285

38. Hinterberger C (2004) Dreidimensionale und tiefengemittelte Large-Eddy-Simulation von Flachwasserströmungen. Ph.D., University of Karlsruhe

39. Rhie CM, Chow WL (1983) Numerical study of the turbulent flow past an airfoil with trailing edge separation. AIAA J 21:1525–1532. doi: 10.2514/3.8284

40. Stone H (1968) Iterative Solution of Implicit Approximations of Multidimensional Partial Differential Equations. SIAM J Numer Anal 5:530–558. doi: 10.1137/0705044

41. Smagorinsky J (1963) General circulation experiments with the primitive equations. Mon Weather Rev 91:99–164. doi: 10.1175/1520-0493(1963)091<0099:GCEWTP>2.3.CO;2

42. Hinterberger C, Fröhlich J, Rodi W (2007) Three-Dimensional and Depth-Averaged Large-Eddy Simulations of Some Shallow Water Flows. J Hydraul Eng. doi: 10.1061/(ASCE)0733-9429(2007)133:8(857)

43. Zhu J (1991) A low-diffusive and oscillation-free convection scheme. Commun Appl Numer Methods 7:225–232. doi: 10.1002/cnm.1630070307

44. Denev JA, Fröhlich J, Bockhorn H (2009) Large eddy simulation of a swirling transverse jet into a crossflow with investigation of scalar transport. Phys Fluids 1994-Present 21:015101. doi: 10.1063/1.3054148

45. Palau-Salvador G, García-Villalba M, Rodi W (2011) Scalar transport from point sources in the flow around a finite-height cylinder. Environ Fluid Mech 11:611–625. doi: 10.1007/s10652-010-9199-3

46. Fröhlich J, García-Villalba M, Rodi W (2007) Scalar Mixing and Large-Scale Coherent Structures in a Turbulent Swirling Jet. Flow Turbul Combust 80:47–59. doi: 10.1007/s10494-007-9121-3

47. García-Villalba M, Palau-Salvador G, Rodi W (2014) Forced Convection Heat Transfer from a Finite-Height Cylinder. Flow Turbul Combust 93:171–187. doi: 10.1007/s10494-014-9543-7

48. Blanckaert K, Graf WH (2001) Mean Flow and Turbulence in Open-Channel Bend. J Hydraul Eng 127:835–847. doi: 10.1061/(ASCE)0733-9429(2001)127:10(835)

List of Figure Captions

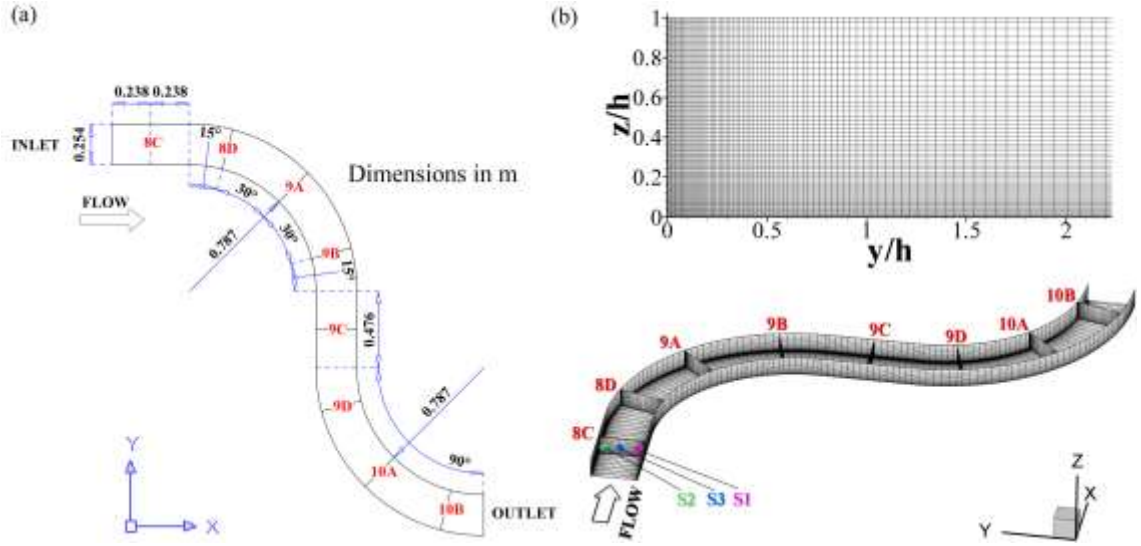

Fig. 1 Computational domain. **a** sketch of the meander used in the experiments (adapted from Chang [24]). **b** Top: detail of the grid used in the LES in the left half of a cross-section. Bottom: view of the grid and the three scalar injections; every 4th grid line is shown

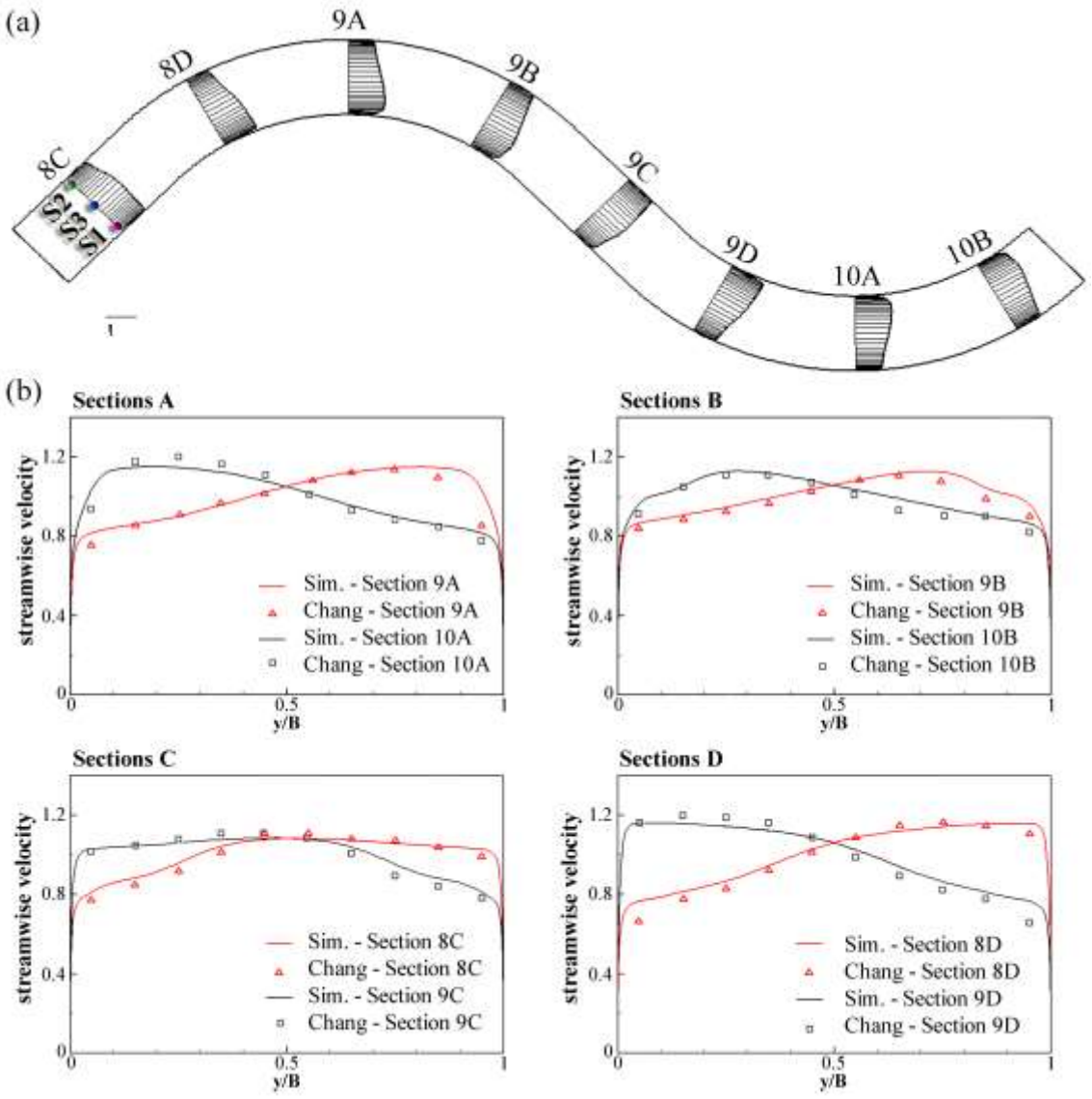

Fig. 2 a depth-averaged mean stream-wise velocity distribution $\overline{u}^h$ along the meander normalized with the bulk velocity U_s. **b** comparison of the $\overline{u}^h$ normalized by U_s with experimental data at selected locations

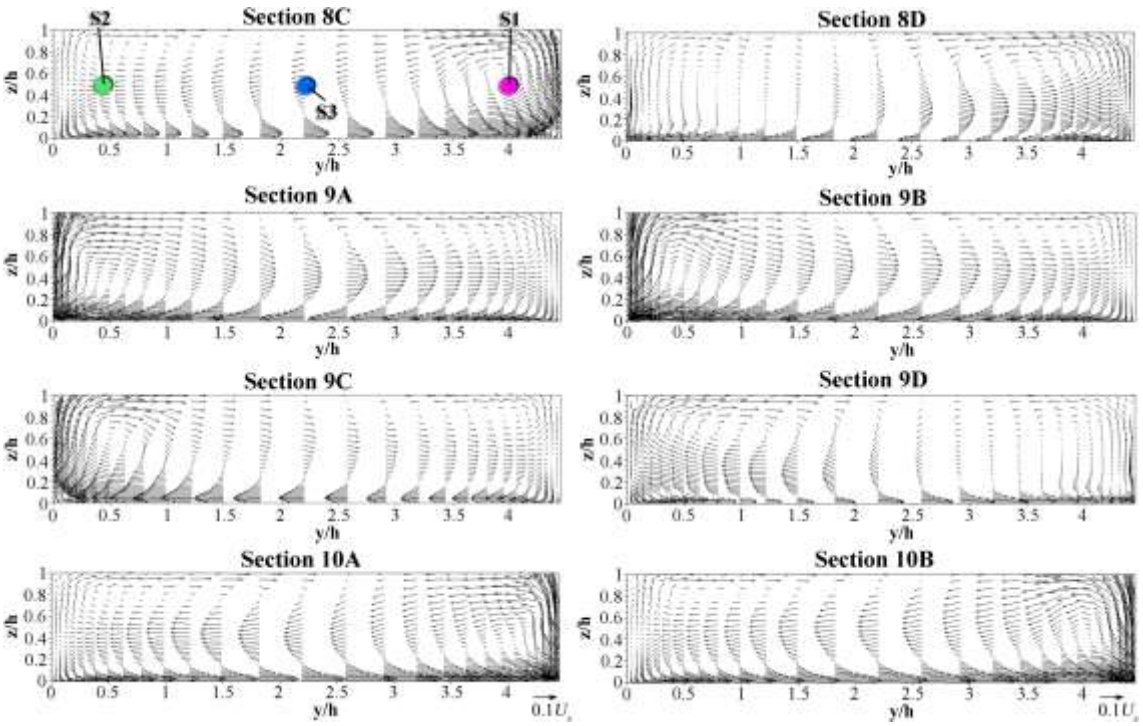

Fig. 3 Mean secondary flow vectors in different cross-sections along the meander normalized by the bulk velocity U_s

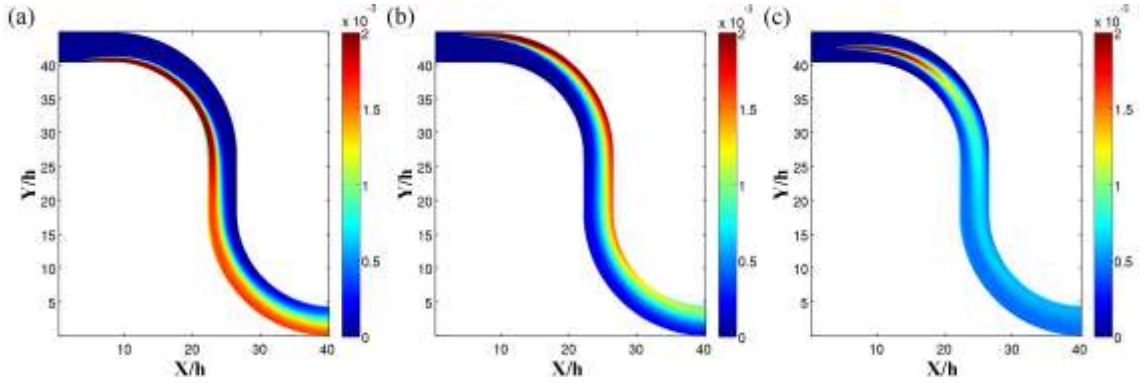

Fig. 4 Depth-averaged mean concentration $\overline{C}^h$ distribution along the meander. **a** S1 (released at x/h = 4.18, y/h = 0.5 and z/h = 0.45); **b** S2 (released at x/h = 4.18, y/h = 0.5 and z/h = 2.23); and **c** S3 (released at x/h = 4.18, y/h = 0.5 and z/h = 4.01)

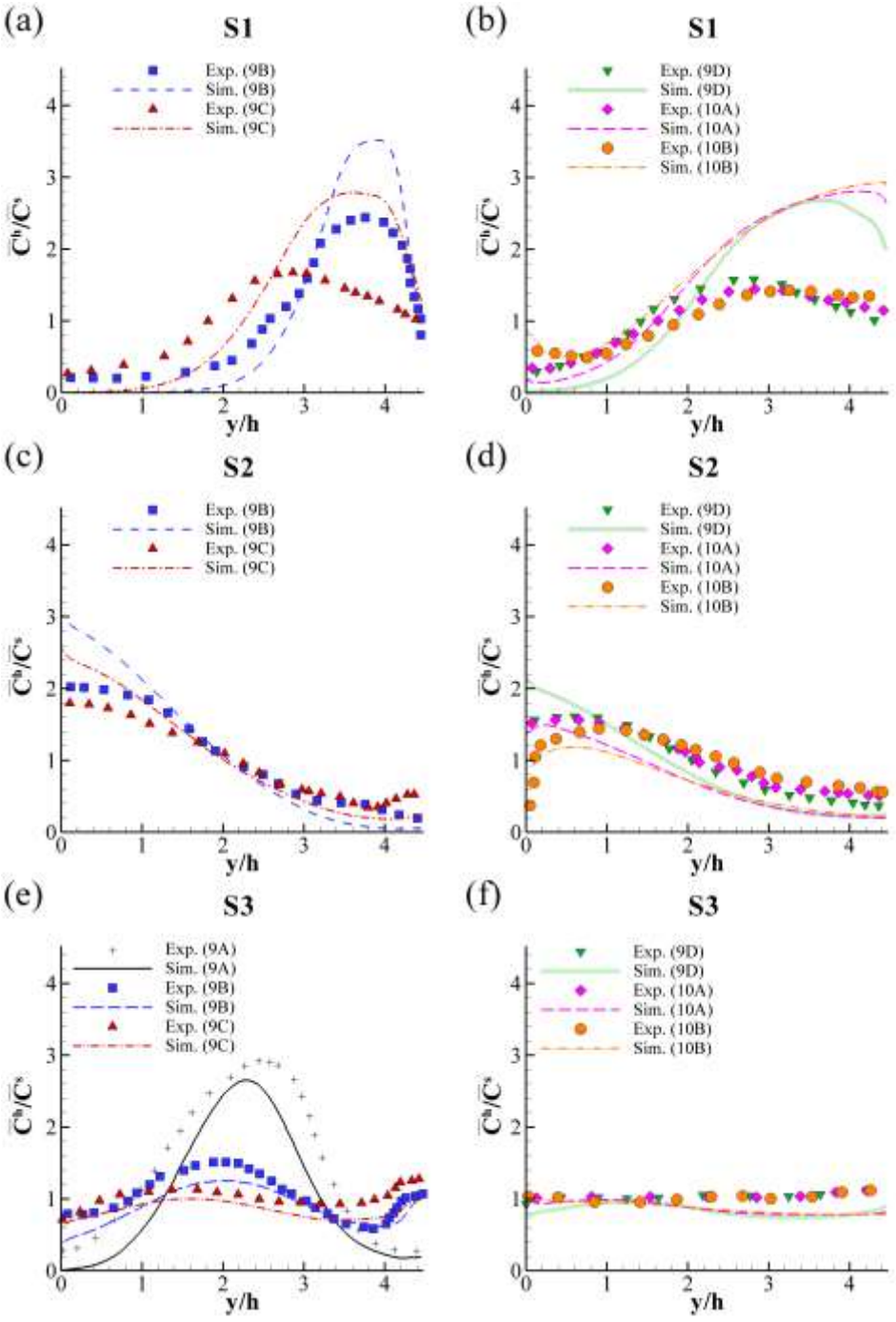

Fig. 5 Depth-averaged mean concentration $\overline{C}^h$ profiles for the three different release locations normalized with the local mean concentration $\overline{C}^s$. Comparison with experimental data at selected locations: S1 (released at x/h = 4.18, y/h = 0.5 and z/h = 0.45), S2 (released at x/h = 4.18, y/h = 0.5 and z/h = 2.23) and S3 (released at x/h = 4.18, y/h = 0.5 and z/h = 4.01)

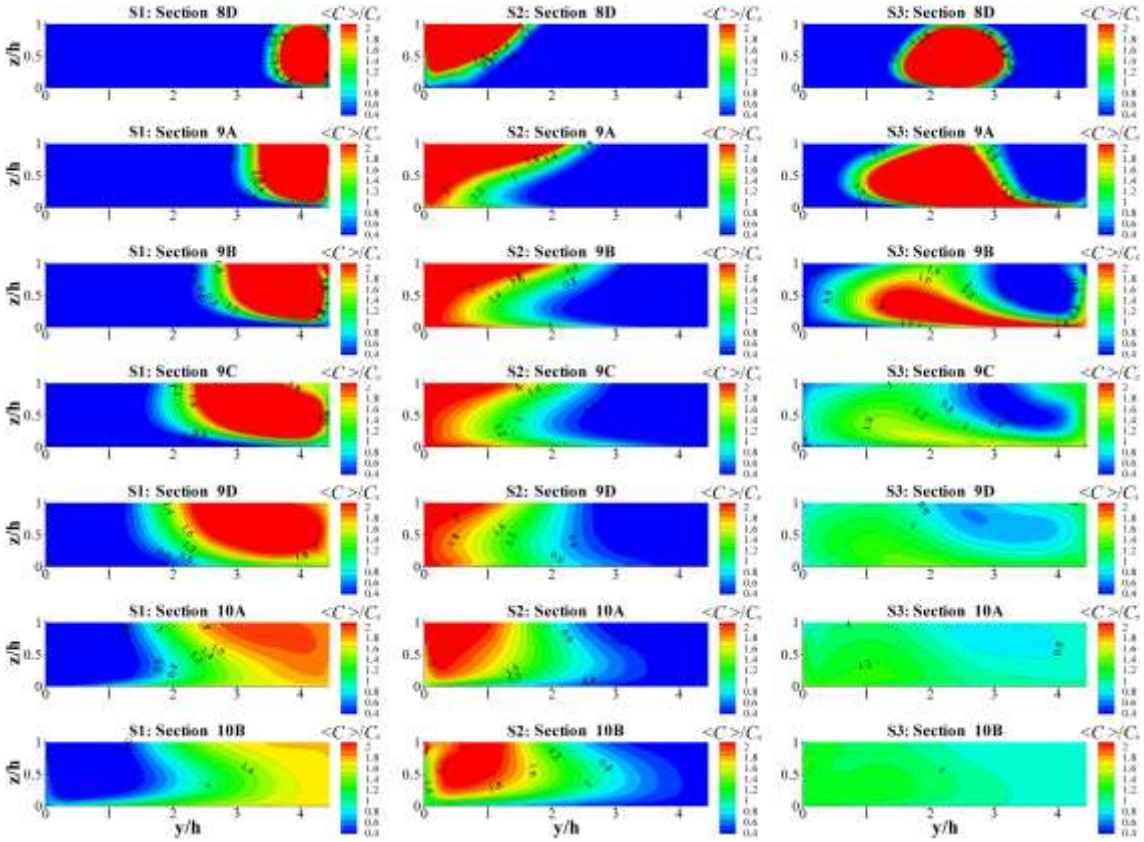

Fig. 6 Mean concentration <*C*> fields normalized with the area-weighted average of the mean concentration C_s in 7 different planes along the meander. Left, S2; middle, S3; and right, S1

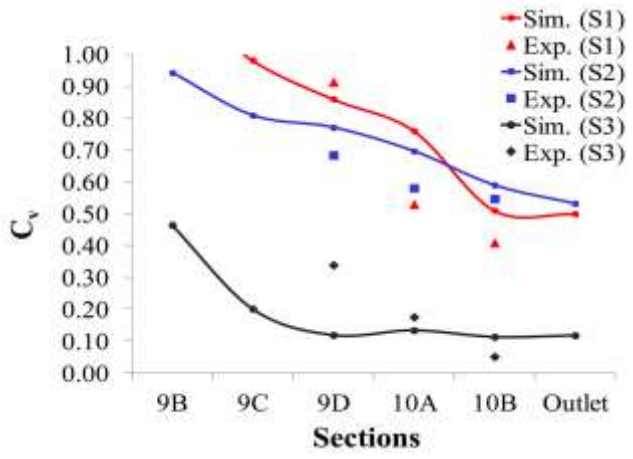

Fig. 7 Mixing coefficient for the three scalar releases. Symbols correspond to the experimental data of Chang [24] and lines correspond to the present data. *Red*, S1. *Blue*, S2. *Black*, S3

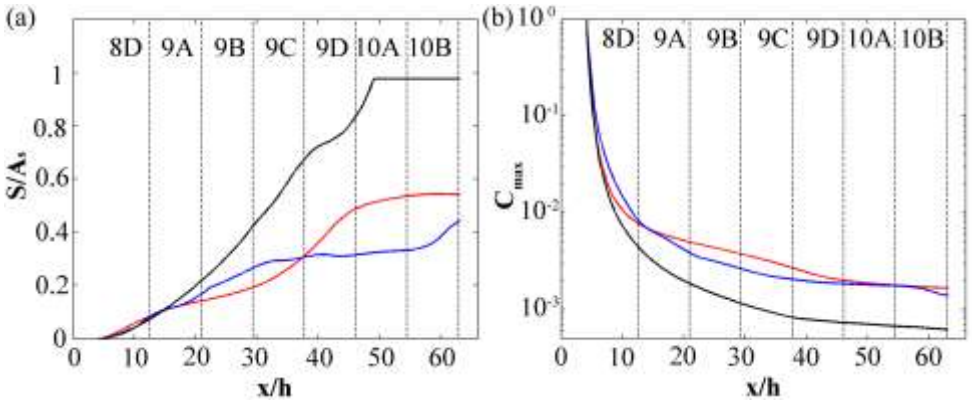

Fig. 8 **a** profiles of half-section S normalized with the flow area A_s ($A_s = h \cdot B$) as a function of x for the three tracer injections. **b** profiles of maximum concentration C_{max} as a function of x for all tracer injections. *Red*, S1. *Blue*, S2. *Black*, S3

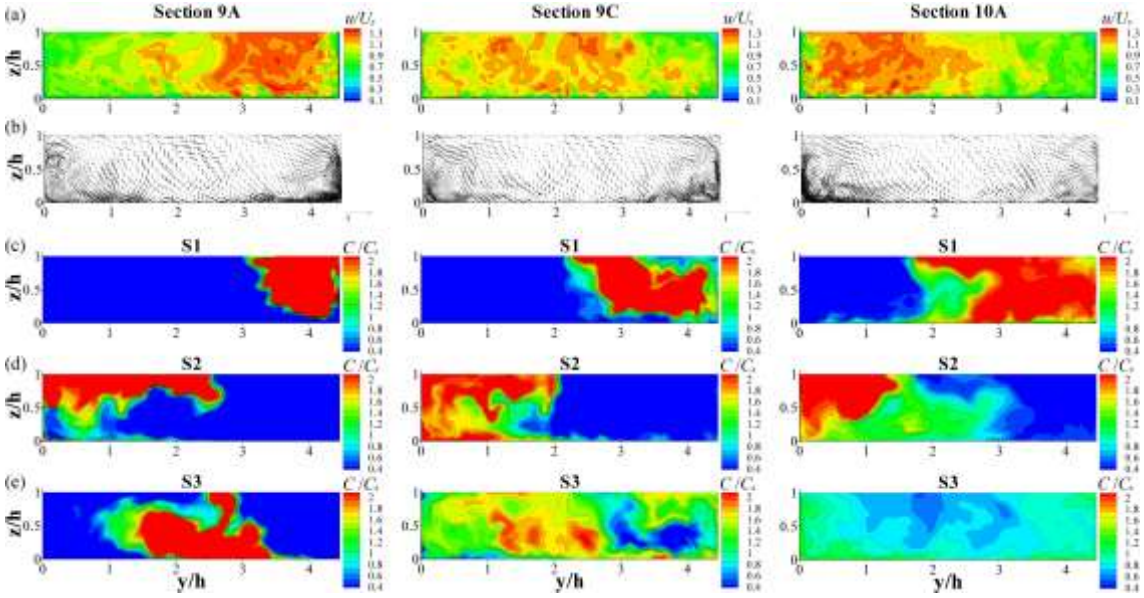

Fig. 9 **a** contours of the instantaneous stream-wise velocity u in different cross-sections normalized by the bulk velocity U_s. **b** instantaneous secondary flow vectors normalized by the bulk velocity U_s. **c** instantaneous concentration C fields normalized with the area-weighted average of the mean concentration C_s. *Left*, Section 9A; *middle*, Section 9C; and *right*, Section 10A

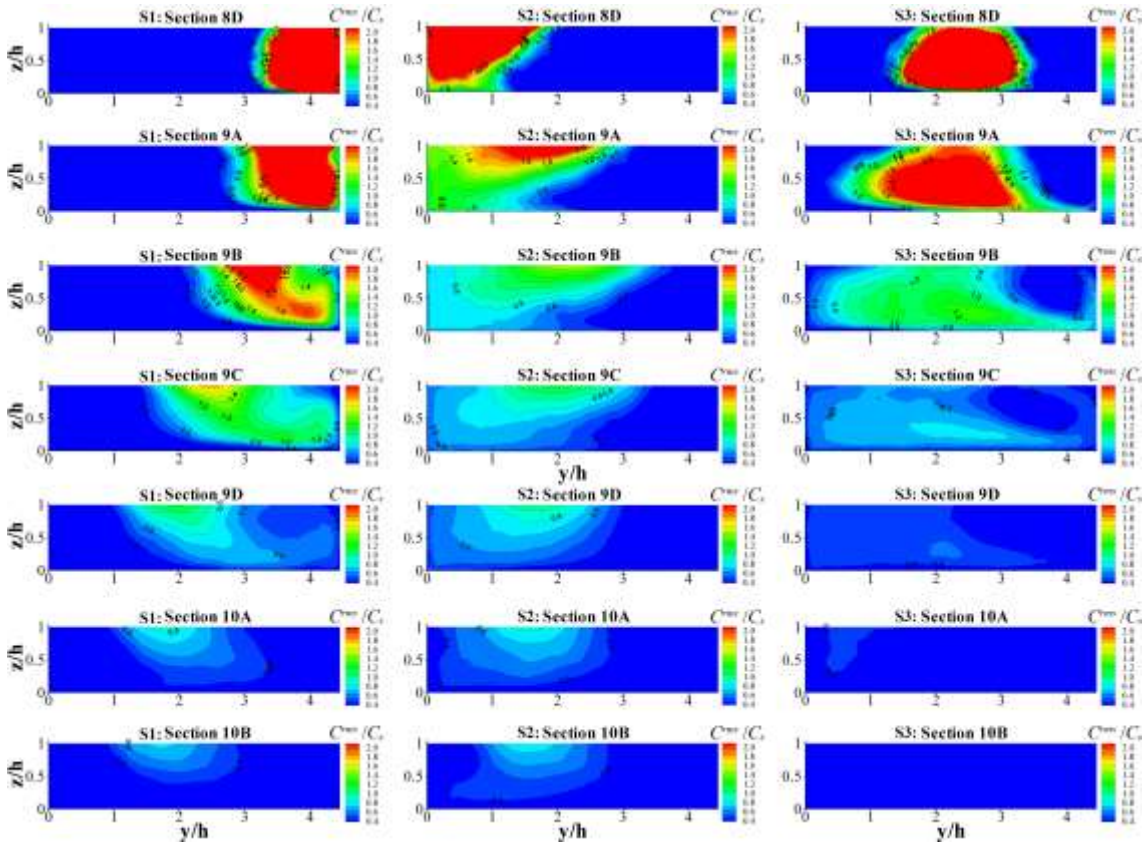

Fig. 10 Root mean square concentration fluctuations C^{rms} fields normalized with the area-weighted average of the mean concentration C_s in 7 different planes along the meander. Left, S2; middle, S3; and right, S1

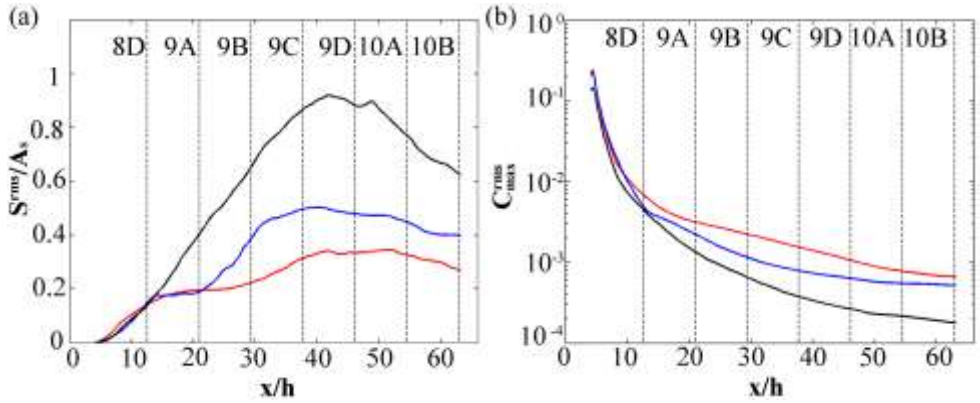

Fig. 11 **a** profiles of half section S^{rms} normalized with the cross-sectional area A_s ($A_s = h \cdot B$) as a function of x for the three tracer injections. **b** profiles of maximum root mean square concentration fluctuations C^{rms}_{max} as a function of x for all tracer injections. *Red*, S1. *Blue*, S2. *Black*, S3ç